PHYSICAL REVIEW E **108**, 054406 (2023)

Collective effects in flow-driven cell migration

Louis González and Andrew Mugler[*]
Department of Physics and Astronomy, University of Pittsburgh, Pittsburgh, Pennsylvania 15260, USA

(Received 5 May 2023; revised 20 September 2023; accepted 17 October 2023; published 13 November 2023)

Autologous chemotaxis is the process in which cells secrete and detect molecules to determine the direction of fluid flow. Experiments and theory suggest that autologous chemotaxis fails at high cell densities because molecules from other cells interfere with a given cell's signal. We investigate autologous chemotaxis using a three-dimensional Monte Carlo-based motility simulation that couples spatial and temporal gradient sensing with cell-cell repulsion. Surprisingly, we find that when temporal gradient sensing dominates, high-density clusters chemotax faster than individual cells. To explain this observation, we propose a mechanism by which temporal gradient sensing allows cells to form a collective sensory unit. We demonstrate using computational fluid mechanics that that this mechanism indeed allows a cluster of cells to outperform single cells in terms of the detected anisotropy of the signal, a finding that we demonstrate with analytic scaling arguments. Our work suggests that collective autologous chemotaxis at high cell densities is possible and requires only known, ubiquitous cell capabilities.

DOI: 10.1103/PhysRevE.108.054406

I. INTRODUCTION

One of the more fascinating ways that cells detect the direction of fluid flow is through a mechanism termed autologous chemotaxis. In autologous chemotaxis, cells secrete and bind to an autocrine factor that diffuses and drifts along the flow lines [1]. More molecules bind to the downstream side of the cell, allowing it to determine the flow direction and consequently migrate downstream along the resulting concentration gradient [1,2]. Autologous chemotaxis is especially relevant in the context of metastatic cancer and has been observed in breast cancer cells [1,3], melanoma cells [1], glioma cells [4], as well as endothelial cells [5].

Experiments have found that autologous chemotaxis fails at high cell density and is overpowered by a competing, density-independent mechanosensing mechanism [3,6]. Theory [7] and simulations [3,7] suggest that the reason for the failure is that, at high cell density, molecules secreted by other cells interfere with a given cell's autologous gradient. Essentially, the signal from all cells produces a background concentration which reduces the relative gradient experienced by any cell. A mean-field calculation based on this argument correctly predicts the cell density at which autologous chemotaxis fails [7].

Nevertheless, in many other biological contexts, cells at high cell density have been shown to detect weak signals, including concentrations [8] and concentration gradients [9,10]. Theory has suggested that they do so by acting collectively [11–15]. Indeed, experiments have shown that collective sensing can lead to the detection of weaker signals [10], or to entirely different behaviors [16], than cells can perform alone. These findings raise the question of whether autologous chemotaxis can benefit from these ubiquitous collective effects, to prevent sensory failure—or even mediate a sensory improvement—at high cell density. This question is particularly relevant to the dense tumor environment in which autologous chemotaxis is principally observed.

Here we combine three-dimensional Monte Carlo simulation, computational fluid mechanics, and theory to investigate the effects of collective sensing on autologous chemotaxis. We perform dynamic cell migration simulations, revealing a regime in which cells chemotax faster as a cluster than as individuals. To explain this regime, we numerically solve the fluid flow and advection-diffusion equations for the concentration secreted by a static configuration of cells, and we find that beyond a crossover cell density, respond more accurately than individual cells, resembling a collective sensing unit. We develop scaling arguments for how the detected signal should scale with cell density, which help explain the numerical findings. Our results reveal a chemotaxis mechanism based entirely on known and ubiquitous ingredients, with potential implications for migration of tumor cells and other cell types in high density environments.

II. RESULTS

A. Motility simulation and collective chemotaxis

We first develop a dynamic simulation of autologous chemotaxis, including molecule secretion in the presence of flow and the ensuing cell motility. Our simulation incorporates only concentration sensing and gradient sensing by individual cells and cell-cell repulsion. We will see that these basic capabilities, ubiquitous among cells of many types, are sufficient to realize autologous chemotaxis and that they lead to a density-mediated crossover from individual to collective chemotaxis in the flow direction.

---

[*] andrew.mugler@pitt.edu

Consider N cells of radius a that each secrete molecules at a rate ν. The molecules diffuse with coefficient D in the presence of a background flow with velocity v. In the next section, for a static configuration of such cells, we will numerically solve for the flow lines and the molecular concentration field. Here, however, to focus on cell dynamics and maintain computational tractability, the simulation makes two important simplifications. First, we reduce cells to point particles on a cubic lattice with spacing given by the cell radius a. Thus, each cell moves to one of six neighboring sites at each time step according to a Monte Carlo scheme, as described shortly. Second, we write the molecular concentration field as the sum of contributions from each cell, where each contribution is approximated as the known single-cell solution obtained as if the cell were isolated [17]. This approximation avoids the need to numerically solve for the flow lines and the concentration field at every time step, and it should be valid for cell densities not too close to the tight-packing limit.

Specifically, we approximate the concentration as $c(\vec{r}) \approx \sum_{j=1}^{N} \tilde{c}(\vec{r}-\vec{r}_j)$, where $\vec{r}_j$ is the position of cell j, and $\tilde{c}$ is the solution to the single-cell problem. That solution obeys the advection-diffusion equation in steady state,

$$0 = \frac{\partial \tilde{c}}{\partial t} = D\nabla^2\tilde{c} - \vec{v}\cdot\vec{\nabla}\tilde{c}, \tag{1}$$

where the flow lines $\vec{v}$ are given by the steady-state solution to the Brinkman equation for flow past a sphere in a porous medium with permeability K [18]. The Brinkman equation is appropriate for the low-Reyolds-number, low-permeability cell environment [1,3]. Because experiments suggest that the Péclet number $\epsilon = va/D$ is small (see below), Eq. (1) was solved previously using ϵ as a perturbation parameter [17]. Choosing $\theta = 0$ as the flow direction far from the cell, the result is

$$\frac{\tilde{c}(\vec{r})}{\bar{c}} = \frac{a}{r} + \frac{\epsilon}{2}\left\{-1 + \frac{\cos\theta}{4}\left[\frac{f(1)}{2r^2/a^2} + f(r/a)\right]\right\}, \tag{2}$$

where $\bar{c} = \nu/4\pi Da$,

$$f(x) = 4 - \frac{4(2\kappa+1)}{x^2} + \frac{2(1+3\kappa+3\kappa^2)}{x^3} + \frac{\kappa^2 e^{1/\kappa}}{x^3}\left[\left(\frac{x^3}{\kappa^3} - \frac{x^2}{\kappa^2} + \frac{2x}{\kappa} - 6\right)e^{-x/\kappa} - \frac{x^4 E_1(x/\kappa)}{\kappa^4}\right], \tag{3}$$

$E_1(y) = \int_1^\infty dt\ e^{-yt}/t$, and $\kappa = \sqrt{K}/a$. We note that $f(1)$ varies between 1 ($\kappa \gg 1$) and 2 ($\kappa \ll 1$).

The parameters are set from experiments as follows. A breast cancer (MDA-MB-231) cell is approximately $a = 10\,\mu\text{m}$ in radius [1,3] and secretes approximately $\nu = 1$ CCL19/21 molecule per second [1,17] which diffuses with approximate coefficient $D = 150\,\mu\text{m}^2/\text{s}$ [2]. The cell density experiments [3] were performed with flow velocity $v = 3\,\mu\text{m/s}$ and permeability $K = 0.1\,\mu\text{m}^2$. We see from these values that the Péclet number $\epsilon = va/D = 0.2$ is indeed small. Nevertheless, while we use $v = 3\,\mu\text{m/s}$ for the numerics in the next section, we lower the flow speed to $v = 0.5\,\mu\text{m/s}$ here, thus lowering the Péclet number further to $\epsilon = 1/30$, in order to maintain the validity of the perturbative solution out to distances much larger than the cell size.

The Monte Carlo scheme accepts or rejects moves according to a pseudopotential and a pseudowork function [19–21]. The pseudopotential is

$$U = \sum_{j=1}^{N}\sum_{k<j}\frac{\lambda^2}{|\vec{r}_j - \vec{r}_k|^2} - \psi_c\sum_{j=1}^{N}\frac{c(\vec{r}_j)}{\bar{c}}. \tag{4}$$

In the first term, closer cell pairs correspond to larger pseudopotential. This term thus corresponds to cell-cell repulsion, with length parameter λ. Cell-cell repulsion occurs in many cell types, often mediated by contact inhibition of locomotion [22]. In the second term, larger concentration values correspond to smaller pseudopotential. This term thus corresponds to concentration sensing with strength ψ_c. The potential difference involved in the Monte Carlo scheme is then equivalent to comparing concentration values from one time step to the next, akin to temporal gradient sensing, as seen in motile bacteria [23,24]. Singularities in the second term from self-energies $\tilde{c}(0)$ are removed because the Monte Carlo scheme considers only potential differences between configurations before and after a cell moves, which contain the same N self-energy terms.

The pseudowork function is

$$W = \psi_g\frac{c(\vec{r}_j + \delta\vec{r}_i) - \bar{c}_j}{\bar{c}_j}, \tag{5}$$

where $\delta\vec{r}_i/a$ are the unit vectors in each of the six directions, and $\bar{c}_j = \sum_{i=1}^{6} c(\vec{r}_j + \delta\vec{r}_i)/6$ is the concentration averaged over these neighboring sites. Equation 5 gives the pseudowork corresponding to the movement of cell j to its neighboring site in direction i. Positive pseudowork means moving to a site whose concentration is higher than the average of all neighboring sites. Equation 5 thus corresponds to gradient sensing with strength ψ_g. Because positive pseudowork means moving to a site whose concentration is higher than the average of all neighboring sites, the pseudowork function biases the motion toward higher concentrations. Because the comparison is done in a single time step, it is spatial (comparing different sides of the cell) rather than temporal (comparing concentrations before and after movement). This process is akin to spatial gradient sensing, as seen in amoeba and yeast [25,26].

Given the pseudopotential and pseudowork terms, the Monte Carlo scheme proceeds as follows [20,21]. At each time step, each cell j moves to its neighboring site i (selected at random) with probability

$$P = \begin{cases} e^{-(\Delta U - W)} & \Delta U - W \geqslant 0 \\ 1 & \Delta U - W < 0, \end{cases} \tag{6}$$

where W is calculated before the move, and U is calculated both after and before the move to give ΔU. The cells are initialized as an N-cell chain along the direction of the flow and move in an unbounded domain.

At low cell density, $\Delta U \to 0$, and W for a move in the flow direction is on the order of $\psi_g\epsilon$. Therefore we set ψ_g to a value on the order of $1/\epsilon$, namely $\psi_g = 10$. We then vary the relative strength of concentration sensing vs gradient sensing by varying ψ_c. To do so in a way that maintains a typical spacing between cells, we consider the pseudopotential between a pair of cells separated by a distance r, which reads $U = \lambda^2/r^2 - 2\psi_c[a/r + \tilde{c}(0)/\bar{c} + \mathcal{O}(\epsilon)]$. This function

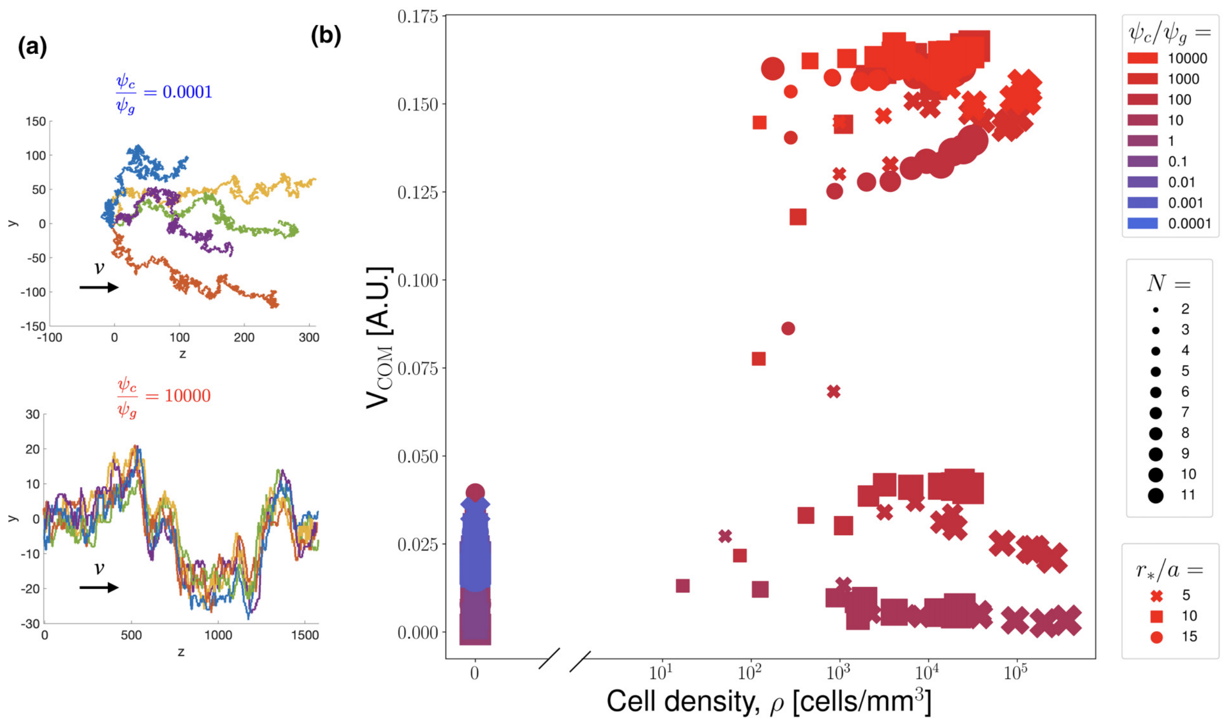

FIG. 1. Motility simulation. (a) Snapshots of $N = 5$ cell trajectories with $r_*/a = 1$, for $\psi_c \ll \psi_g$ (top) and $\psi_c \gg \psi_g$ (bottom). Cells drift in the flow direction individually (top) or collectively (bottom). Note the difference in axes' scales: the migration distance is much farther for the bottom plot. (b) Center-of-mass velocity vs cell density. As ψ_c/ψ_g increases (blue to red), density increases as cells transition to collective migration. The velocity first decreases, then increases, indicating that collective chemotaxis outperforms individual chemotaxis. Here $a = 10\ \mu\text{m}$, $\nu = 1\ \text{s}^{-1}$, $D = 150\ \mu\text{m}^2/\text{s}$, $v = 0.5\ \mu\text{m/s}$, $K = 0.1\ \mu\text{m}^2$, $\psi_g = 10$, and $\lambda = \max(\sqrt{\psi_c a r_*}, 10a)$.

has a minimum at $r_* = \lambda^2/\psi_c a$. Therefore, for a given r_*, as we vary ψ_c, we set λ via this expression until it becomes too small to mediate the repulsion. Specifically, we find that $\lambda = \max(\sqrt{\psi_c a r_*}, 10a)$ is sufficient to prevent cells from cohering permanently (which arrests migration).

Figure 1 shows the simulation results. Focusing first on typical cell trajectories [Fig. 1(a)], we see that for $\psi_c \ll \psi_g$ (top), cells execute diffusive trajectories that drift in the flow direction but do not stay together. This is because at low ψ_c, cells lack the coattraction mediated by concentration sensing and feel only repulsion when close; once separated, they execute autologous chemotaxis individually by spatial gradient sensing. In contrast, we see that for $\psi_c \gg \psi_g$ (bottom), cells remain as a cohesive group whose center of mass executes a diffusive trajectory that drifts in the flow direction. This is because at high ψ_c, concentration sensing mediates both a coattraction and the movement toward maximal concentration; due to the flow, the highest concentration is downstream of the group, resulting in collective autologous chemotaxis.

In Fig. 1(b), we plot the center-of-mass velocity in the flow direction v_{COM} vs the cell density ρ, as we vary ψ_c/ψ_g (color), r_* (shape), and N (size). The center-of-mass velocity is computed as the displacement in the flow direction divided by the number of time steps, for 10^4 time steps, averaged across the N cells and across five simulation trials. The cell density is computed as the inverse of the average cell-cell spacing. In simulations for which the average cell-cell spacing does not saturate within 10^4 time steps, cells are determined to be diffusing away from each other indefinitely, and the cell density is set to $\rho = 0$.

Consistent with Fig. 1(a), we see in Fig. 1(b) that the results are relatively insensitive to r_* and N, and are primarily tuned by ψ_c/ψ_g. Specifically, we see that for $\psi_c \ll \psi_g$ (blue, lower left), $\rho = 0$, and cells move with a characteristic v_{COM} indicative of individual autologous chemotaxis. For $\psi_c \sim \psi_g$ (purple, lower right), ρ increases as the coattraction sets in, and v_{COM} slightly decreases. This finding is consistent with the experimental observation that autologous chemotaxis begins to fail at high cell densities [3,6]. Interestingly, for $\psi_c \gg \psi_g$ (red, upper right), ρ stays high, and v_{COM} significantly increases, above that for $\psi_c \ll \psi_g$. Because high ψ_c corresponds to collective autologous chemotaxis as described above, this finding suggests that collective autologous chemotaxis can outperform individual chemotaxis at high cell densities. To understand this result further, we turn to computational fluid dynamics in the next section.

B. Numerical computation and crossover cell density

The simulations indicate that for $\psi_c \ll \psi_g$, cells chemotax individually, whereas for $\psi_c \gg \psi_g$ cells chemotax collectively. Individual chemotaxis corresponds to a cell comparing concentration values at different points on its surface and biasing migration in the direction of the highest concentration [Eq. (5)]. For a spherical cell of radius a, this surface bias is quantified using the dimensionless anisotropy measure

[12,17,27]

$$A_I = \frac{\int d\Omega c(a,\theta,\phi)\cos\theta}{\int d\Omega' c(a,\theta',\phi')}, \tag{7}$$

where $c(a,\theta,\phi)$ is the molecular concentration at the cell surface, and $d\Omega = d\phi d\theta \sin\theta$ is the solid angle element. The cosine extracts the asymmetry between the downstream ($\theta = 0$) and upstream ($\theta = \pi$) sides of the cell such that $A_I > 0$ for a downstream gradient and $A_I < 0$ for an upstream gradient.

In contrast, collective chemotaxis corresponds to cells seeking the highest concentration values and moving as a cohesive unit [Eq. (4)]. Information sensed by individual cells is propagated to other cells via movement, given that cells are coattracted. We therefore hypothesize that this cohesive unit performs a collective analog of the computation in Eq. (7). In terms of the surface concentration c_j averaged around cell j, this collective anisotropy measure reads

$$A_C = \frac{\sum_{j=1}^N c_j \cos\theta_j}{\sum_{k=1}^N c_k}, \tag{8}$$

where the surface integral has been replaced by a sum over the N cells, and θ_j is the angle the cell makes with the flow direction relative to the collective's center of mass.

To test our hypothesis about collective information gathering, we calculate Eqs. (7) and (8) numerically for a static configuration of cells. Focusing on a static configuration allows us to separate the sensing from the dynamics and to relax the simplifying assumptions of the simulations. If the sensory measures in Eqs. (7) and (8) are the primary drivers of chemotaxis, we expect the dependence of A_I and A_C on cell density to be similar to that of the migration velocity in Fig. 1(b).

To evaluate Eqs. (7) and (8), we obtain the concentration field $c(\vec{r})$ at all points in space by numerically solving the fluid dynamics and advection-diffusion equations. Specifically, we solve the steady-state Brinkman equation to find the velocity field, which provides the advection term in the steady-state advection-diffusion equation for the molecular concentration [Eq. (1)]. We use a finite-element computational fluid dynamics package (COMSOL) to solve both equations [3,7]. Details are provided in our previous work [7], and the code for the present work is freely available [28].

To vary the cell density, we keep the volume of the system constant while varying the number of cells N. This protocol mimics the microfluidic experiments used to investigate autologous chemotaxis [3], and indeed we consider a system with dimensions similar to the microfluidic chamber: a rectangular box domain of length L, width W, and height H, where the flow is in the direction of L [Fig. 2(a)]. Cells are placed uniform-randomly throughout the box, ensuring that one cell is in the center, and that the cells do not overlap with one another or with the boundaries of the box. Both the individual and collective anisotropy measures are averaged over random configurations of cells in the domain. The individual anisotropy [Eq. (7)] is computed from c at the surface of the center cell [7] [Fig. 2(a), right], while the collective anisotropy [Eq. (8)] is computed from the surface-averaged c_j of each cell [Fig. 2(a), left].

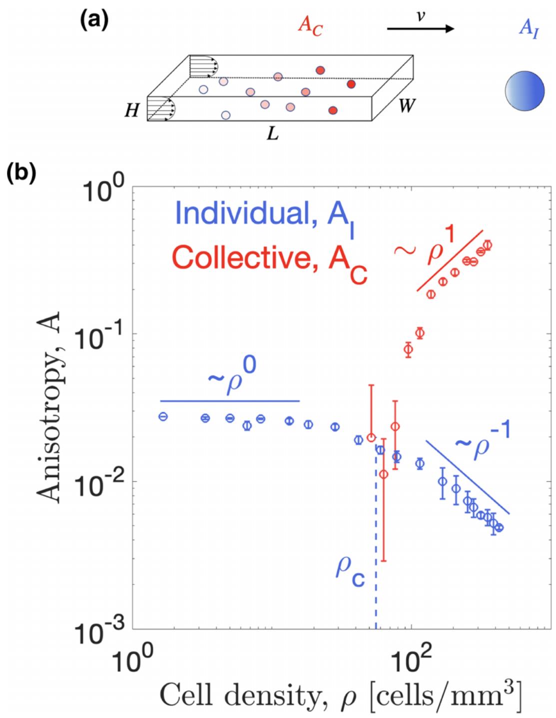

FIG. 2. Numerical computation using fluid dynamics software. (a) Schematic of cells randomly placed in domain with dimensions L, W, and H, and flow in the L direction. Collective anisotropy A_C considers the average surface concentration at each cell (left), whereas individual anisotropy A_I considers the angular variation in the surface concentration around the center cell (right). (b) Individual and collective anisotropy vs cell density from numerics (mean and standard error over five trials with random cell configurations), compared with predicted scalings. Here $a = 10$ μm, $\nu = 1$ s^{-1}, $D = 150$ μm^2/s, $v = 3$ μm/s, $K = 0.1$ μm^2, $L = 3$ mm, $W = 2$ mm, and $H = 100$ μm.

As in the motility simulations, we use $a = 10$ μm [1,3], $\nu = 1$/s [1,17], $D = 150$ μm^2/s [2], and $K = 0.1$ μm^2 [3]. From the cell density experiments [3], we obtain $v = 3$ μm/s and a chamber of length $L = 3$ mm, width $W \approx 2$ mm, and height $H \sim 100$ μm.

The numerical anisotropies A_I and A_C as a function of cell density $\rho = N/LWH$ are shown in Fig. 2(b) (data points). We see that the individual anisotropy A_I begins to decrease as the cell density increases (blue), consistent with the initial decrease in the migration velocity in the simulations [Fig. 1(b)]. Indeed, autologous chemotaxis has been observed in the range 50–250 cell/mm^{-3} [3], and individual sensing is thought to break down toward the top of that range [3,7], consistent with Fig. 2(b). We also see in Fig. 2(b) that at higher cell densities, the collective anisotropy A_C increases with cell density (red), again consistent with the ultimate increase in the migration velocity in the simulations [Fig. 1(b)]. Figure 2(b) demonstrates that collective sensing outperforms individual sensing ($A_C > A_I$) above a crossover density on the order of $\rho \sim 50$ cells/mm^{-3}. The typical cell spacing at the crossover density, $\rho^{-1/3} \sim 270$ μm, is much larger than a cell diameter, $2a \approx 20$ μm, implying that collective effects could be beneficial well before reaching the tight-packing limit typical of tissues and tumors.

Altogether, our findings at the level of migration [Fig. 1(b)] are consistent with our findings at the level of anisotropy [Fig. 2(b)]. This suggests that the sensory measures in Eqs. (7) and (8) are the primary drivers of chemotaxis and supports the hypothesis that movement with coattraction can mediate collective information gathering. Figure 2(b) also reveals clear scaling laws that govern sensory information. To understand the physics behind these scaling laws, we turn to theory in the next section.

C. Theory and scaling laws

To understand the scaling behaviors seen in the numerical results of Fig. 2(b), we derive the scaling laws of anisotropy with cell density from the physics of molecular diffusion. We first review the result for the individual anisotropy from previous work, and we then present the derivation for the collective anisotropy.

1. *Individual sensing*

In previous work [7], we showed that the individual anisotropy in Eq. (7) could be approximated as $A_I \approx (n_d - n_u)/n_d$, where n_u and n_d are the numbers of molecules detected by the upstream and downstream halves of the cell, respectively. Specifically,

$$n_u = \frac{\nu}{D/a^2 + v/a}, \tag{9}$$

where we have constructed the molecule number as a ratio of the rates of molecules entering (by secretion ν) and leaving (by diffusion D or flow v, respectively) the cell half. The expression for n_d lacks the v_0/a term because molecules lost to flow downstream are replenished by those lost to flow from the upstream half. As a result, the anisotropy simplifies to $A_I \approx \epsilon$ for small Péclet number $\epsilon = v_0 a/D$ [7]. A more rigorous calculation confirms this scaling, yielding $A_I = \epsilon/8$ [17].

We further showed using a mean-field argument that, in the presence of identical cells at a density ρ, the anisotropy for a given cell scales as

$$A_I = \frac{\epsilon/8}{1 + \rho/\rho_c}, \tag{10}$$

where $\rho_c = \epsilon/4\pi a^2 L$, and L is the system size in the flow direction. The critical density ρ_c is the cell density beyond which sensing begins to fail due to the presence of molecules secreted by other cells. We see from Eq. (10) that the individual anisotropy A_I should scale as ρ^0 for $\rho \ll \rho_c$, and as ρ^{-1} for $\rho \gg \rho_c$, explaining the numerics in Fig. 2(b) (blue), as seen previously [7].

2. *Collective sensing*

Now consider an entire collective of cells as the sensory unit (Fig. 3). We define the collective anisotropy in Eq. (8) here in terms of molecule numbers,

$$A_C = \frac{1}{n_T}\sum_{j=1}^{N} n_j \cos\theta_j, \tag{11}$$

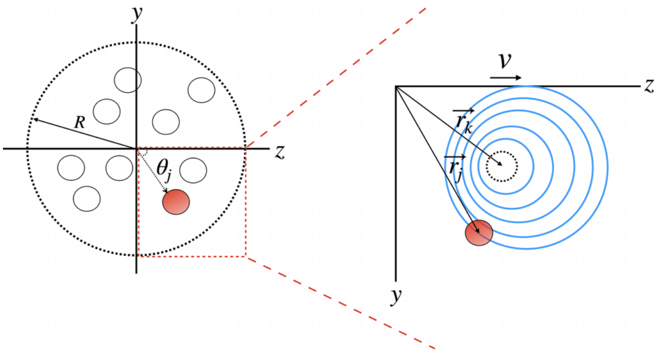

FIG. 3. Schematic of the cell collective. Left: a particular cell j makes an angle θ_j with the flow direction $\hat{z}$, relative to the collective's center of mass. The collective's volume is characterized by a length-scale R. Right: Molecules secreted by any other cell k drift in the flow direction a distance vt and diffuse isotropically a characteristic distance $\sqrt{Dt}$, tracing out a spherical shell.

where n_j is the number of molecules within the volume of the jth cell, and n_T is the total number of molecules within the volume of the collective (Fig. 3, left). We estimate n_j and n_T following Eq. (9),

$$n_j = \frac{\nu + \nu_j}{D/a^2 + v/a}, \tag{12}$$

$$n_T = \frac{N\nu}{D/R^2 + v/R}. \tag{13}$$

In Eq. (12), ν_j is the rate of arrival, to cell j, of molecules secreted by other cells. In Eq. (13), R is the radius of the collective; for a spherical arrangement, it is related to the cell density as $\rho = N/(4\pi R^3/3)$.

To find the molecule arrival rate ν_j, we consider a specific cell k in the collective that acts as a source of these molecules, and we will ultimately sum over k. In a time t, a molecule released from cell k drifts in the flow direction a distance vt and diffuses isotropically a characteristic distance $\sqrt{Dt}$, tracing out a spherical shell described by $|\vec{r} - \vec{r}_k - vt\hat{z}|^2 = Dt$, where $\hat{z}$ is the flow direction, and $\vec{r}_k$ is the position of cell k (Fig. 3, right). This shell will reach cell j when $\vec{r} = \vec{r}_j$, giving $|\vec{r}_j - \vec{r}_k|^2 - 2vt(z_j - z_k) + v^2t^2 = Dt$. Rescaling time as $\tau \equiv tD/a^2$ and recalling that $\epsilon = va/D$, this equation becomes $|\vec{r}_j - \vec{r}_k|^2/a^2 - 2\epsilon\tau(z_j - z_k)/a + \epsilon^2\tau^2 = \tau$. Because the Péclet number is small ($\epsilon \ll 1$), we neglect the quadratic term, giving a rescaled arrival time of $\tau = |\vec{r}_j - \vec{r}_k|^2/[a^2 + 2\epsilon a(z_j - z_k)]$. At this time, the shell has a radius $\sqrt{Dt}$, and the likelihood of the molecule reaching cell j is the ratio of the cell's cross-sectional area πa^2 to the shell's surface area $4\pi Dt$, or $a^2/4Dt = 1/4\tau$. Thus, the arrival rate of molecules at cell j is the secretion rate ν multiplied by this likelihood and summed over k,

$$\nu_j = \nu \sum_{k \neq j} \frac{a^2 + 2\epsilon a(z_j - z_k)}{4|\vec{r}_j - \vec{r}_k|^2}. \tag{14}$$

We insert Eq. (14) into Eq. (12), and Eqs. (12) and (13) into Eq. (11). For the purposes of obtaining a scaling, we approximate the sums as integrals. Doing so, and writing

Eqs. (12) and (13) in terms of ϵ, we obtain

$$A_C \approx \frac{a^2[1+(R/a)\epsilon]}{NR^2(1+\epsilon)} \int \frac{d^3r_j}{R^3/N} \cos\theta_j \times \left[1 + \int \frac{d^3r_k}{R^3/N} \frac{a^2 + 2\epsilon a(r_j\cos\theta_j - r_k\cos\theta_k)}{4|\vec{r}_j - \vec{r}_k|^2}\right]. \tag{15}$$

Here we have used $z = r\cos\theta$ and scaled the volume element d^3r by the typical volume occupied by one cell, which goes as R^3/N. Within the large square brackets in Eq. (15), any term that does not depend on θ_j will vanish by symmetry when integrated against the $\cos\theta_j$ outside. Therefore, we isolate the middle term of the $\vec{r}_k$ integral [29],

$$A_C \approx \frac{\epsilon a^3 N[1+(R/a)\epsilon]}{2R^8(1+\epsilon)} \int d^3r_j d^3r_k \frac{r_j\cos^2\theta_j}{|\vec{r}_j - \vec{r}_k|^2}. \tag{16}$$

In the prefactor of Eq. (16), we may neglect the additive terms proportional to ϵ as long as R/a is not too large. In the integral in Eq. (16), we can understand how the result should scale with R without performing the integration: the volume elements contribute factors of R^3 each because the integration extends out to $r = R$; and the numerator and denominator contribute factors of R and R^{-2}, respectively. Altogether, we have $A_C \sim \epsilon a^3 N/R^3$, or

$$A_C \sim \epsilon a^3 \rho, \tag{17}$$

where we have recognized $\rho \sim N/R^3$ as the cell density.

Equation (17) is our main result for how the collective anisotropy should scale with system properties. Several features make intuitive sense. First, the collective anisotropy should vanish as the cell density ρ gets small. The reason is that when cells are far apart, each cell detects the same number of molecules (its own), and the collective computation yields no information on upstream-downstream molecule imbalance. Second, the collective anisotropy should increase with the Péclet number $\epsilon = va/D$, as the individual anisotropy does [Eq. (10)]. The reason is that a larger ϵ (e.g., via a faster flow speed v) naturally increases the molecule imbalance.

We see from Eq. (17) that A_C should scale with ρ, explaining the numerics in Fig. 2(b) (red). We also expect the scaling in Eq. (17) to break down when the typical distance between cells $\rho^{-1/3}$ becomes larger than the smallest lengthscale of the domain (here, H). We write this condition as $\rho^{-1/3} > \alpha H$, where α is a constant that we expect to be of order unity. Rearranging, we have $\rho < (\alpha H)^{-3}$. Figure 2(b) (red) shows that the numerics indeed become especially sensitive to cell arrangement, leading to large variability in A_C, for $\rho \lesssim 10^2$ mm^{-3}, corresponding to $\alpha \approx 2.1$, which is indeed of order unity.

III. DISCUSSION

We have demonstrated that collective effects allow cells at high density to detect fluid flow and migrate downstream using autologous chemotaxis. Indeed, using theory, numerics, and simulation, we have shown that whereas individual autologous chemotaxis worsens with cell density, collective autologous chemotaxis improves. We derived and validated the associated scaling laws and identified a crossover cell density at which the optimal strategy switches from individual to collective. We observed this crossover in motility simulations invoking only cell-cell repulsion, and concentration and gradient sensing by single cells.

Collective effects are ubiquitous in cell biology, and previous work has shown that they confer behaviors beyond those available to single cells. Collective effects can sharpen a cell behavior: in epithelial cells, collective sensing allows groups of cells to detect shallower gradients than any single cell can detect alone [10]. Collective effects can reverse a behavior: in lymphocytes, single cells migrate down a gradient, whereas groups of cells migrate up [16]. Here, we have found that collective effects can "rescue" a behavior: as cell density increases, individual sensing fails, but then collective sensing takes over and ultimately surpasses individual sensing. This is a potentially new interplay between single-cell and collective sensing that may suggest a density-dependent switch between two sensory regimes.

Sensory computations in single cells are performed by biochemical networks. It is not obvious that analogous computations can be performed collectively by groups of cells, especially when those cells are separated in space. In principle, the components of such a biochemical computation would need to be relayed diffusively among cells [10,13]. Surprisingly, here we have found that in the case of autologous chemotaxis, the sensed signal and the relay signal can be the same component. The secreted molecule drifts with the flow, and thus its concentration is the sensed signal. At the same time, the secreted molecule originates from the cells themselves, and thus its concentration contains information on the cells' configuration; it is the relay signal. Even beyond sensing, the secreted molecule aids in collective migration because it acts as the coattractant. These simultaneous capabilities prevent the need for complicated extracellular secretion networks. Indeed, for the particular task of flow sensing by autologous chemotaxis, our results demonstrate that collective chemotaxis can be achieved with a single molecular species, and with the simple ingredients of concentration sensing and cell-cell repulsion.

Collective migration has not been observed in experiments on autologous chemotaxis performed to date. Perhaps this is because autologous chemotaxis has been discovered exclusively in eukaryotic cells, which are generally thought to migrate by comparing concentrations in space, whereas our mechanism requires comparing concentrations in time. Alternatively, perhaps this is because at high cell densities, where collective effects would dominate, it has been shown that a separate mechanism takes over that reverses migration, at least in breast cancer cells [3]. Nevertheless, the mechanism we reveal here is not specific to eukaryotic cells. Smaller cells such as bacteria use temporal sensing to track gradients. For such cells, in the presence of a flow, we predict that secreting and sensing a molecule is sufficient to produce efficient, collective migration in the flow direction.

ACKNOWLEDGMENT

This work was supported by National Science Foundation Grants No. PHY-2118561 and No. MCB-2118037.

[1] J. D. Shields, M. E. Fleury, C. Yong, A. A. Tomei, G. J. Randolph, and M. A. Swartz, Cancer cells **11**, 526 (2007).

[2] M. E. Fleury, K. C. Boardman, and M. A. Swartz, Biophys. J. **91**, 113 (2006).

[3] W. J. Polacheck, J. L. Charest, and R. D. Kamm, Proc. Natl. Acad. Sci. USA **108**, 11115 (2011).

[4] J. M. Munson, R. V. Bellamkonda, and M. A. Swartz, Cancer Res. **73**, 1536 (2013).

[5] C.-L. E. Helm, M. E. Fleury, A. H. Zisch, F. Boschetti, and M. A. Swartz, Proc. Natl. Acad. Sci. USA **102**, 15779 (2005).

[6] W. J. Polacheck, A. E. German, A. Mammoto, D. E. Ingber, and R. D. Kamm, Proc. Natl. Acad. Sci. USA **111**, 2447 (2014).

[7] M. Vennettilli, L. González, N. Hilgert, and A. Mugler, Phys. Rev. E **106**, 024413 (2022).

[8] T. Gregor, D. W. Tank, E. F. Wieschaus, and W. Bialek, Cell **130**, 153 (2007).

[9] W. J. Rosoff, J. S. Urbach, M. A. Esrick, R. G. McAllister, L. J. Richards, and G. J. Goodhill, Nat. Neurosci. **7**, 678 (2004).

[10] D. Ellison, A. Mugler, M. D. Brennan, S. H. Lee, R. J. Huebner, E. R. Shamir, L. A. Woo, J. Kim, P. Amar, I. Nemenman *et al.*, Proc. Natl. Acad. Sci. USA **113**, E679 (2016).

[11] T. Erdmann, M. Howard, and P. R. Ten Wolde, Phys. Rev. Lett. **103**, 258101 (2009).

[12] J. Varennes, S. Fancher, B. Han, and A. Mugler, Phys. Rev. Lett. **119**, 188101 (2017).

[13] A. Mugler, A. Levchenko, and I. Nemenman, Proc. Natl. Acad. Sci. USA **113**, E689 (2016).

[14] B. A. Camley, J. Zimmermann, H. Levine, and W.-J. Rappel, PLoS Comput. Biol. **12**, e1005008 (2016).

[15] S. Fancher and A. Mugler, Phys. Rev. Lett. **118**, 078101 (2017).

[16] G. Malet-Engra, W. Yu, A. Oldani, J. Rey-Barroso, N. S. Gov, G. Scita, and L. Dupré, Curr. Biol. **25**, 242 (2015).

[17] S. Fancher, M. Vennettilli, N. Hilgert, and A. Mugler, Phys. Rev. Lett. **124**, 168101 (2020).

[18] B. Barman, Indian J. Pure Appl. Math. **27**, 1249 (1996).

[19] A. Szabó, R. Ünnep, E. Méhes, W. Twal, W. Argraves, Y. Cao, and A. Czirók, Phys. Biol. **7**, 046007 (2010).

[20] J. Varennes, B. Han, and A. Mugler, Biophys. J. **111**, 640 (2016).

[21] U. Roy and A. Mugler, Phys. Rev. E **103**, 032410 (2021).

[22] R. Mayor and C. Carmona-Fontaine, Trends Cell Biol. **20**, 319 (2010).

[23] R. M. Macnab and D. E. Koshland, Jr., Proc. Natl. Acad. Sci. USA **69**, 2509 (1972).

[24] H. Mao, P. S. Cremer, and M. D. Manson, Proc. Natl. Acad. Sci. USA **100**, 5449 (2003).

[25] R. A. Arkowitz, Trends Cell Biol. **9**, 20 (1999).

[26] J. A. Swanson and D. L. Taylor, Cell **28**, 225 (1982).

[27] R. G. Endres and N. S. Wingreen, Proc. Natl. Acad. Sci. USA **105**, 15749 (2008).

[28] Code is available at https://github.com/gonzalezlouis/Autologous-3.

[29] Neglecting the first and last terms in the second line of Eq. (15) ignores the dependence of $|\vec{r}_j - \vec{r}_k|^2$ on θ_j. We validate this uncontrolled approximation post hoc when checking our results against numerics in Sec. II B.